AD_____

Award Number: W81XWH-06-1-0443

TITLE: Combined MR and Optical Imaging System for Noninvasive Tumor Characterization and Quantification of Oxygenation Gain Factor in a Breast Cancer Animal Model

PRINCIPAL INVESTIGATOR: Roshanak Shafiiha, Ph.D.

CONTRACTING ORGANIZATION: University of California
Irvine, CA 92697

REPORT DATE: June 2007

TYPE OF REPORT: Annual

PREPARED FOR: U.S. Army Medical Research and Materiel Command
Fort Detrick, Maryland 21702-5012

REPORT DOCUMENTATION PAGE

Form Approved
OMB No. 0704-0188

1. REPORT DATE *(DD-MM-YYYY)*	**2. REPORT TYPE**	**3. DATES COVERED** *(From - To)*
01/06/07	Annual	19 May 2006 – 18 May 2007

4. TITLE AND SUBTITLE

Combined MR and Optical Imaging System for Noninvasive Tumor Characterization and Quantification of Oxygenation Gain Factor in a Breast Cancer Animal Model

5a. CONTRACT NUMBER

5b. GRANT NUMBER
W81XWH-06-1-0443

5c. PROGRAM ELEMENT NUMBER

6. AUTHOR(S)
Roshanak Shafiiha, Ph.D.

E-Mail: shafiiha@uci.edu

5d. PROJECT NUMBER

5e. TASK NUMBER

5f. WORK UNIT NUMBER

7. PERFORMING ORGANIZATION NAME(S) AND ADDRESS(ES)

University of California
Irvine, CA 92697

8. PERFORMING ORGANIZATION REPORT NUMBER

9. SPONSORING / MONITORING AGENCY NAME(S) AND ADDRESS(ES)
U.S. Army Medical Research and Materiel Command
Fort Detrick, Maryland 21702-5012

10. SPONSOR/MONITOR'S ACRONYM(S)

11. SPONSOR/MONITOR'S REPORT NUMBER(S)

12. DISTRIBUTION / AVAILABILITY STATEMENT
Approved for Public Release; Distribution Unlimited

13. SUPPLEMENTARY NOTES

14. ABSTRACT: This study proposes to modify and improve an existing MR-compatible optical tomography system that is used for non-invasive tumor characterization and provides higher sensitivity and specificity for cancer imaging. The proposed research will conduct animal studies to evaluate the system's performance in distinguishing malignant from benign tumors in vivo. Additional experiments will be designed to assess the method's sensitivity to quantifying oxygenation gain factor in breast tumors. This investigation will have important implications for studies identifying tumor's hypoxic regions. Tumor hypoxia is believed to be strongly associated with tumor progression, prognosis, and resistance to therapy. In the first year of this multidisciplinary postdoctoral training grant, the principal investigator acquires training in breast cancer and dynamic contrast enhanced MRI. The major focus is on optical imaging system development/improvement and performance evaluation through phantom studies. We managed to increase the data acquisition speed by a factor of 10, which enabled us to perform dynamic contrast enhanced diffuse optical tomography on phantoms for the first time.

15. SUBJECT TERMS
Optical Tomography, Magnetic Resonance Imaging (MRI), Oxygenation Gain Factor, Breast Cancer

16. SECURITY CLASSIFICATION OF:			**17. LIMITATION OF ABSTRACT**	**18. NUMBER OF PAGES**	**19a. NAME OF RESPONSIBLE PERSON**
a. REPORT	**b. ABSTRACT**	**c. THIS PAGE**			USAMRMC
U	U	U	UU	25	**19b. TELEPHONE NUMBER** *(include area code)*

Table of Contents

INTRODUCTION

In the last decade a variety of multi-modality imaging techniques have been developed to obtain complementary information and cross-validate measurements to investigate the differences in the physiological properties of benign and malignant tumors, and hence make tumor assessment more reliable. Magnetic resonance imaging (MRI) and near-infrared diffuse optics are non-invasive techniques that provide complementary structural and functional physiological information. Comparison and complementary use of these two imaging modalities has the potential to enhance our understanding of the complex biological processes that are associated with tumor transformation, growth, and hemodynamics.

The proposed study will integrate MRI with near-infrared (NIR) diffuse optical spectroscopy (DOS) and diffuse optical tomography (DOT) to develop an MR-compatible three-dimensional (3D) spectroscopic diffuse optical tomography (SDOT) system to improve spatial localization and quantification of tumor optical properties. Animal studies will be conducted to evaluate the system's performance in distinguishing malignant breast tumors from benign ones in vivo. Experiments also will be designed to assess the method's sensitivity to quantifying oxygenation gain factor (OGF) in breast.

In this study, our first hypothesis is that congruent spectroscopic diffuse optical tomography and MRI will lead to better understanding and evaluation of the physical properties to which optical imaging is sensitive. In addition to this, with the complementary information obtained from the MRI and improved SDOT reconstruction algorithm, the chromophore concentrations for benign and malignant tumors will be evaluated and compared. This leads us to our second hypothesis, which is: a congruent SDOT and MRI system for tumor imaging will lead to an improved specificity in tumor characterization. Finally, our third hypothesis is: a congruent SDOT and MRI system for tumor imaging will lead to an improved quantification of the hypoxic regions in heterogeneous tumors and better prognosis in breast cancer.

BODY

In this multi-disciplinary post-doctoral training grant, we will evaluate the potential of a hybrid MR and optical imaging system in tumor characterization and quantification of oxygenation gain factor in a breast cancer animal model. During the first phase of the project, accuracy and quality of the optical imaging technique will be improved by modifying the existing data acquisition schemes and comparison and complementary use of MRI. In the next phase, the system will be employed to test the above-mentioned hypotheses. Four specific aims were proposed to achieve the overall goals of the project:

Aim 1. MR-SDOT system development

a. Integration of the DOS with the existing prototype MR-DOT system
b. Multi-wavelength parallel detection for reduced data acquisition time
c. Expansion of the optical probe from a single-ring 2D probe to a three-ring volumetric imaging system

Aim 2. Evaluation of the MR-SDOT system through phantom studies

Aim 3. Evaluation of the MR-SDOT system through animal studies

a. Evaluation of the physiological properties of different types of tumors
b. Quantification of oxygenation gain factor

Aim 4. Data analysis and Comparison

Statement of Work

To achieve the abovementioned specific aims, following tasks needs to be completed as outlined in the approved Statement of Work. The tasks that were proposed to be partially or fully accomplished during the first year of the award period are indicated in bold.

Task 1. Develop the necessary background in cancer biology and technical skills in MRI (Months 1-24)

a. Audit classes and attend seminars on cancer biology (Months 1-18).

b. Acquire technical expertise in DCE-MRI and RF coil design (Months 13-24).

c. Training in animal handling and preparation during the preliminary studies (Months 13-24)

Task 2. MR-SDOT system development (Months 1-18)

a. Integration of the DOS with the UCI prototype MR-DOT system (Months 1-6).

b. Multi-wavelength parallel detection for reduced data acquisition time (Months 7-12).

c. Expansion of the optical probe from a single-ring 2D probe to a three-ring volumetric imaging system (Months 13-18).

Task 3. Evaluation of the MR-SDOT system through phantom studies (Months 1-18)

a. Using homogeneous phantoms with different chromophore concentrations (Months 1-18).

b. Using inhomogeneous phantoms with different sizes of inclusion (Months 1-18).

Task 4. Evaluation of the MR-SDOT system through preliminary animal studies (Months 19-24)

a. Preliminary MR-SDOT measurements on 10 ENU induced rats to optimize the measurement parameters and MR-optics co-registration for the 5th task (Months 19-21).

b. Preliminary congruent DCE-MRI and SDOT studies on 10 ENU induced rats to optimize the imaging parameters for the 5th task (Months 22-24).

Task 5. Evaluation of the MR-SDOT system through pre-clinical animal studies (Months 25-36)

a. Congruent DCE-MRI and SDOT measurements on 50 ENU induced rats for hypothesis testing (Months 25-32).

b. Data analysis to evaluate the physical properties of different types of tumor (Months 25-32)

c. Data analysis for OGF quantification in different types of tumor (Months 25-32).

d. Comparison with pathology results and ROC analysis (Month 32-36).

Tasks 1.a. Training stage: Audit classes and attend seminars on cancer biology

To develop the necessary background in cancer biology, the principal investigator has audited a class in "*Molecular Biology of Cancer*", offered by Dr. Eva Lee (secondary mentor) from the Department of Biological Sciences at UCI (BIOSCI 125). The class discussed topics in:

I. The Hallmarks of Cancer
II. Tumor Viruses
III. Chemical Carcinogenesis
IV. Human Cancer Genes
V. Stem Cells and Cancer Stem Cells
VI. Targeted Cancer Therapies

The principal investigator also attended weekly seminars offered by the Center for Functional Onco-Imaging (CFOI) and Beckman Laser Institute (BLI). The speakers talk about the state of the art onco-imaging techniques and novel applications of optics in biomedical research.

As a member of The National Cancer Institute's Network for Translational Research in Optical Imaging (NTROI), the principal investigator gets the opportunity to attend the annual retreats in June, where team members from academic and industrial organizations get together to focus on creating new instruments specifically designed for detecting breast cancer and monitoring breast cancer therapies. Technologies are based on optical imaging and the integration of optics with MRI and x-ray

mammography.

The principal investigator became a member of the UCI's Cancer Center and receives regular updates and information on their seminars and activities. She also attended one of the Breast Tumor Board presentations by the Division of Surgical Oncology.

Tasks 1.b. Training stage: Acquire technical training in DCE-MRI

Acquiring technical expertise in dynamic contrast enhanced-magnetic resonance imaging (DCE-MRI) was originally proposed as part of the training in the second year of the award. However, the Principal investigator managed to accomplish this task during the first year, where she received basic training in data acquisition (adjustment of dynamic pulse sequences and synchronization with contrast agent injection) and conducted a dynamic animal experiment herself.

Task 2.a. Optical imaging system development: Integration of DOS with DOT

In the first year, one of the tasks to be completed was to incorporate optical spectroscopic capabilities to a pre-existing hybrid animal imaging system based on MRI and DOT for better chromophore identification and improved concentration quantification [1]. We proposed to replace the broadband source with a number of NIR laser diodes to provide higher intensity per wavelength, resulting in reduced integration time at the detector and hence improved data acquisition speed. Simulation studies reported previously in the proposal showed that 14 wavelengths can sample the entire NIR spectrum with reasonable accuracy. To put this into practice, we made a discrete-broadband source consisting of 14 laser diodes with wavelengths: 658, 682, 760, 785, 810, 830, 840, 850, 870, 880, 900, 915, 950, and 980 nm (figure 1). These lasers are only DC biased. We do not need to modulate them. For testing purposes, before integrating the discrete-broadband source to DOT system, we replaced the broadband source in DOS instrument with the discrete-broadband source and performed single-source single-detector DOS phantom and tissue studies to validate the results. A 14 to 1 fiber bundle collects the light from laser diodes and sends them to the phantom/tissue using direct contact.

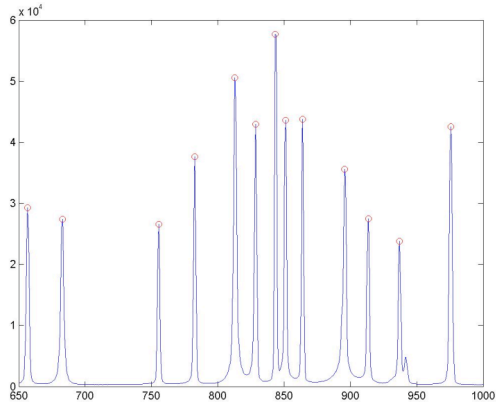

Figure 1. Discrete-broadband spectrum: Photon count vs. wavelength (nm)

Problems faced:

The broadband measurement is calibrated at each measurement session using an integrating sphere with a nearly flat spectral response over the wavelength region of interest [2]. For the discrete-broadband measurement we were not able to use the integration sphere because of the multi-mode nature of the laser light. After trying different calibration standards, we concluded that the best way to calibrate the discrete-broadband measurement is using a flat-surface calibration standard instead of a sphere.

Turning the lasers off and on during a discrete-broadband measurement makes them unstable in intensity, resulting in significant inaccuracy in reconstructed values for chromophore concentrations. Keeping the diodes constantly on improves the stability, but makes the fiber-tissue contact point hot and uncomfortable. We need a fast shutter mechanism to block the light during the idle time. Operating the laser diode in constant power mode using photodiode feedback also improves the stability of the laser

diode and reduces the intensity fluctuations from 15% to 5%. In the next year of the award, we are planning to implement both of these methods to bring the stability of the diodes to a tolerable level.

Task 2.b. Optical imaging system development: Multi-frequency parallel detection

To reduce the data acquisition time, we have developed a multi-frequency parallel detection scheme during the first year of the award (figure 2). A network analyzer is used to sequentially modulate the laser diodes with the desired frequency (in the range of 100 ~ 300 MHz). On the detection site, light is transmitted to the photomultiplier tubes (PMTs) through neutral density filters. Output of each PMT is amplified and mixed with the RF signal generated by a programmable RF frequency synthesizer. This frequency synthesizer is programmed to generate a signal at a frequency of 5 kHz above the modulation frequency of the laser diodes. Outputs of the mixers are then low-pass filtered and captured by the 8-channel data acquisition (DAQ) card simultaneously. Phase and amplitude of the detected 5 kHz signals are then recovered digitally using MATLAB signal processing toolbox. The DAQ card is a National Instrument 8-channel dynamic signal acquisition module (PXI-4472) with 24-bit resolution, 110 dB dynamic range, 45 kHz bandwidth, and sampling rate of 102.4 kS/s. This card is installed in a National Instrument PXI-1031 chassis that communicates with the computer through a National Instrument PXI-8330 MXI-3 interface. We have been able to accurately recover the phase and amplitude of the signals as low as -80 dBm by this method. This parallel concurrent technique reduces the data acquisition time remarkably. Also the use of network analyzer and frequency synthesizer provides great flexibility in the selection of the modulation frequency. We have achieved the acquisition speed of ~ 30 second per frequency, per wavelength. Before, each acquisition took ~ 5 minutes!

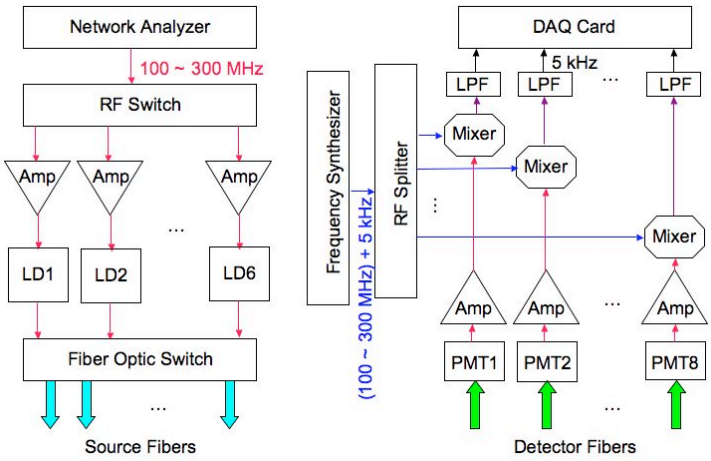

Figure 2. The schematic of the multi-frequency modulation and detection circuitry

Currently there are 6 laser diodes with wavelengths 658, 680, 758, 808, 830, and 850 nm in our system. With this method we can provide slightly different modulation frequency for each laser diode and measure the phase and amplitude of the detected signals. Since each receiver will be locked to its own currier frequency, output signals will be detected simultaneously without any cross-talk among different wavelengths.

We have tested and optimized the performance of the system through phantom studies as stated in the next section.

Problems faced:

Originally we proposed *multi-wavelength* parallel detection in order to simultaneously modulate the laser diodes. In practice, when we modulate all 6 lasers at the same time, the RF noise of the system increases significantly and causes an out-of-tolerance condition for imaging. We have ordered an RF shield box to be customized for our application (Lindgren RF Enclosures, Inc). All the lasers will be located in the box with filtered terminals to power supplies and other instruments. The shielding performance of the box is 120 dB+ to eliminate the RF noise and make the multi-wavelength parallel detection possible.

Task 3. System evaluation through phantom studies

Multi-compartmental solid and liquid phantoms were used at each developmental stage to evaluate the performance of the system. Different homogeneous and inhomogeneous solid and liquid phantoms simulating tissue optical properties were constructed. Solid compartments were constructed using the method described by Firbank *et al*. [3]. Liquid compartments are made of varying concentrations of Intralipid (%10, F. K. Clayton, NC) and Indian ink (Winsor & Newton, England) in water. Details of the system calibration and image reconstruction have been thoroughly discussed in [4].

In addition to regular phantom studies, due to significant improvement in data acquisition speed, for the first time, we were able to conduct a series of dynamic contrast enhanced DOT and MR-DOT phantom studies using indocyanine green (ICG) [5]. Our analysis shows that ICG kinetics curves obtained by the frequency domain DOT system have the potential to characterize the tumor permeability. We also investigated the use of structural a priori information obtained from MRI in DCE-DOT reconstruction and corresponding effects on the calculation of physiological parameters.

KEY RESEARCH ACCOMPLISHMENTS

- Training of the principal investigator in cancer biology
- Training of the principal investigator in DCE-MRI
- Optical imaging system development: significant reduction in data acquisition time (factor of 10)
- Evaluation of the high-speed system through phantom studies
- Dynamic contrast enhanced DOT and MR-DOT phantom studies using ICG

REPORTABLE OUTCOMES

M. B. Unlu, O. Birgul, **R. Shafiiha**, and G. Gulsen, "Variability of Indocyanine Green Kinetics and Using Structural a priori Information in Dynamic Contrast Enhanced Diffuse Optical Tomography (DCE-DOT)", submitted to *Physics in Medicine and Biology*, June 2007.

CONCLUSION

In the first year of the award period, the specific aims were mostly focused on training of the PI in biology and breast cancer, optical imaging system development/improvement, and performance evaluation through phantom studies. We managed to increase the data acquisition speed significantly (~ 10 times faster than before), which enabled us to perform dynamic contrast enhanced diffuse optical tomography on phantoms for the first time.

Major challenges we encountered during the first year were RF noise reduction in the system and integration of the discrete-broadband spectroscopy to the existing optical tomography system, which are still under development and will be implemented in the near future.

Changes on future schedule:

The principal investigator completed the DCE-MRI training during the first year of the award period (originally proposed for the second year). So in the next year she can re-allocate some time to complete the broadband integration and testing.

So What?

The recent improvement in data acquisition speed opens up new doors for the continuation of our MR-DOT studies. Dynamic contrast enhanced diffuse optical tomography (DCE-DOT) allows the study

of kinetics of the ICG in tumors and normal tissues. It has been demonstrated that ICG has different wash-in and wash-out properties between benign and malignant tumors [6-7]. For example, malignant tumors exhibit a slower wash-out rate compared to benign tumors and normal tissue. Our phantom studies and simulations show that the ICG kinetics curves obtained by the frequency domain DOT system have the potential to characterize the tumor permeability. Such a hybrid MR-optics system that can monitor the enhancement kinetics of an MR (Gd-DPTA) and an optical (ICG) contrast agent has a great potential for increasing specificity in tumor characterization.

REFERENCES

1. F. Bevilacqua, A. J. Berger, A. E. Cerussi, D. Jakubowski, and B. J. Tromberg, "Broadband absorption spectroscopy in turbid media by combined frequency-domain and steady-state methods", *Applied Optics*, 39(34), 6498–6507 (2000).
2. D. B. Jakubowski, A. E. Cerussi, F. Bevilacqua, N. Shah, D. Hsiang, J. Butler, and B. J. Tromberg, "Monitoring neoadjuvant chemotherapy in breast cancer using quantitative diffuse optical spectroscopy: a case study", *Journal of Biomedical Optics*, 9(1), 230-238 (2004).
3. M. Firbank, M. Oda, D.T. Deply, "An improved design for a stable and reproducible phantom material for use in near-infrared spectroscopy and imaging", *Physics in Medicine and Biology*, 40, 955-961 (1995).
4. G. Gulsen, O. Birgul, M. B. Unlu, R. Shafiiha, and O. Nalcioglu, "Combined diffuse optical tomography (OT) and MRI system for cancer imaging in small animals", Technology in Cancer Research Treatment, 5(4), 351-363 (2006).
5. M. B. Unlu, O. Birgul, R. Shafiiha, and G. Gulsen, "Variability of Indocyanine Green Kinetics and Using Structural a priori Information in Dynamic Contrast Enhanced Diffuse Optical Tomography (DCE-DOT)", submitted to *Physics in Medicine and Biology*, June 2007.
6. V. Ntziachristos, A.G. Yodh, M. Schnall, and B. Chance, "Concurrent MRI and diffuse optical tomography of breast after indocyanine green enhancement", *National Academy of Sciences*, 97(6), 2767-2772 (2000).
7. X. Intes, J. Ripoll, Y. Chen, S. Nioka, A. G. Yodh, and B. Chance, "In vivo continuous-wave optical breast imaging enhanced with Indocyanine Green", *Medical Physics*, 30(6), 1039-1047 (2003).

APPENDICES

Reprints of the documents listed in reportable outcomes section.

Variability of Indocyanine Green Kinetics and Using Structural *a priori* Information in Dynamic Contrast Enhanced Diffuse Optical Tomography (DCE-DOT)

Mehmet Burcin Unlu[1], Ozlem Birgul, Roshanak Shafiiha, and Gultekin Gulsen

Tu and Yuen Center for Functional Onco-Imaging, University of California, Irvine, CA 92697, USA

E-mail: munlu@uci.edu

Abstract.

We investigated 1)the variability of the indocyanine green kinetics (ICG) within the same subject and between different subjects changing the size of the imaging region, the location and the size of the inclusion, 2)the use of structural *a priori* information to reduce the variability. We performed simulation and phantom studies for this purpose. In the simulations, we used a two-compartmental model to describe the ICG transport and obtained pharmacokinetic parameters. The wash-in and the wash-out parameters showed a wide variation i.e. 60% and 95% respectively. Moreover, time to reach the peak ICG concentration was different within different cases. When structural *a priori* information was used in the reconstructions, these variations were reduced to 29%, 15%. We also performed a phantom study to validate the use of structural priors in dynamic reconstructions. A 63-*mm*-diameter solid phantom that had a 15-*mm*-diameter cylindrical inclusion was used. A dye-intralipid-water mixture was circulated through the phantom while the diffuse optical tomography measurements were acquired in 30-second steps. The phantom study showed that the wash-in and wash-out parameters were immune to systematic errors introduced by wrong selection the structural priors, e.g. a 30% error in the diameter of the inclusion caused only 2% change in wash-in rate and 4% change in the wash-out rate.

PACS numbers: 87.90.+y

Keywords: Dynamic imaging, diffuse optical tomography, contrast enhancement, indocyanine green, two-compartmental model, reconstruction, computer simulation
Submitted to: *Phys. Med. Biol.*

1. Introduction

Diffuse optical tomography (DOT) can detect the abnormalities in the tissue due to endogenous contrast changes (Gibson et al. 2005). For example in the cancerous breast tissue, the endogenous absorption contrast arises due to different hemoglobin content of the tumor. An additional contrast mechanism is the change in the cellular and organelle density and size. These cellular and subcellular changes cause an increase in the scattering properties of the diseased region (Thomsen & Tatman 1998), (Mourant et al. 1998). It is well established that the endogenous contrast changes can be up to two or three times higher than the healthy tissue (Cerussi et al. 2006). Still, it would be desirable to use exogenous contrast agents in order to increase the contrast between the healthy and diseased tissue and have a better characterization and localization of the abnormalities, very much like in the field of nuclear imaging and magnetic resonance imaging (MRI).

In the Near Infrared (NIR) range the most widely used contrast agent is indocyanine green (ICG). It is approved by the FDA and has been used in the medical field since 1956. ICG is a blood pool agent that binds to plasma proteins (Yoneya et al. 1998), therefore, it is confined to the vascular compartment and behaves as a macromolecular contrast agent with a low vascular permeability. The transport rate of the contrast agent between extravascular and intravascular space is determined by the permeability of the microvessels, their surface area, and blood flow. It has been demonstrated that the ICG has different wash-in and wash-out properties between benign and malignant tumors (Ntziachristos et al. 2000), (Intes et al. 2003). For example, malignant tumors exhibit a slower wash-out rate compared to benign tumors and normal tissue.

Dynamic contrast enhanced diffuse optical tomography (DCE-DOT) allows the study of kinetics of the ICG in tumors and normal tissues. The data are composed of a series of images acquired before and after the injection of ICG. Measured optical flux can be used to generate images of ICG concentration vs. time, C(t), that can then evaluated to extract physiological parameters. Absorption contrast enhancement can be analyzed using a two-compartmental pharmacokinetic model that is described by (Tofts & Kermode 1991).

In recent years, there have been several theoretical and experimental studies of the kinetics of ICG in the tissue. (Gurfinkel et al. 2000) presented a double exponential, four-parameter model to describe uptake of ICG and employed a fluorescence reflectance imaging system for the measurements in small animal models. However, they did not detect a difference in the ICG uptake rates between normal and neoplastic tissue. Later, (Cuccia et al. 2003) used a six-parameter pharmokinetic model and presented a study of the dynamics of ICG in an adenocarcinoma rat tumor model by use of diffuse optical spectroscopy coregistered with MRI. They found differences in the ICG uptake between necrotic and edematous tumors. (Ntziachristos et al. 2000) reported the first results on the uptake of ICG in vivo in the human breast. In their study, a concurrent MRI and frequency domain DOT examination of the human breast was performed. (Intes

et al. 2003) investigated the uptake of ICG by breast tumors using a continuous wave DOT system. (Alacam et al. 2005), (Alacam, Yazici, Intes & Chance 2006) used an extended Kalman filter scheme to analyze small-animal ICG pharmokinetics data given in (Cuccia et al. 2003). (Alacam, Yazici, Intes, Nioka & Chance 2006) presented a study in three breast cancer patients. They observed differences in the ICG concentrations in plasma and the extravascular compartments.

In this study, we use a frequency domain DOT system to study ICG kinetics. Although the absorption information is sufficient to calculate the ICG kinetics, the scattering map must also be reconstructed simultaneously due to the cross talk in measurements of the optical parameters. In addition to this, in parallel to recent developments in nano-oncology, optical imaging systems that can monitor changes in absorption and scattering simultaneously have become very attractive (Ferrari 2005, Jain 2005, Yezhelyev et al. 2006). There have been extensive work on contrast agents that can increase the optical absorption and scattering contrast simultaneously (Malicka et al. 2003).

The major problems on the road to the use of DOT in tumor diagnosis is that it suffers from low spatial resolution and limited depth penetration (Pogue et al. 2000, Song et al. 2002, Pogue et al. 2002, Pogue et al. 2006). In this study, to find the corresponding effects of these limitations on the analysis of the ICG kinetic curves, we performed several simulation and phantom studies. In the simulations, we investigated two questions: 1) how the calculated ICG curve depended on the size and position of the inclusion as well as the size of the imaging region? 2) how the use of structural *a priori* information effected the calculation of the ICG curve? The answer to the first question was closely related to the the inter-subject and intra-subject dependency of the calculated wash-in and wash-out rates of the ICG curves. To our knowledge, this question had not been answered before. The use of structural priors in DOT reconstruction has been widely discussed in the literature and it requires the segmentation of the discretization domain into regions (Dehghani et al. 2006, Dehghani et al. 2003, Brooksby et al. 2005, Li et al. 2003, Li et al. 2007, Intes et al. 2004). This procedure makes it possible to use some constraints in the inverse problem and, as a result, an accurate determination of the average optical parameters in segmented regions can be achieved. A potential failure of the use of structural priors is incorrect segmentation. Therefore, we performed a phantom experiment to investigate the effect of incorrect segmentation on the dynamic absorption coefficient curves and answered the second question. We used the structural priors in the analysis of DCE-DOT data for the first time in the literature.

2. Methods

2.1. Modeling of ICG Kinetics

ICG transport in tissue can be described using a two compartmental model given by (Tofts & Kermode 1991), (Cuccia et al. 2003). The model consists of an intravascular (or

plasma) compartment and an extravascular compartment. Extravascular compartment is the leakage space within the interstitial space of the tissue.

Net flow into the extravascular compartment is

$$\frac{dC_e}{dt} = K^{trans}C_p - k_{ep}C_e \tag{1}$$

where C_p and C_e are the contrast agent concentrations in the plasma and extravascular compartment. $K^{trans}(sec^{-1})$ is the transfer constant that defines the flux rate between the blood plasma and extravascular compartment, and the rate constant $k_{ep}(sec^{-1})$ describes the back flux from extravascular compartment to blood plasma. These parameters are related to each other by the equation, $k_{ep} = K^{Trans}/v_e$ where v_e is the extravascular compartment fractional volume.

The net flow from plasma to extravascular compartment and kidneys/liver can be approximated by a biexponential decay:

$$C_p(t) = A_1 \exp(-\alpha_1 t) + A_2 \exp(-\alpha_2 t) \tag{2}$$

where A_1, A_2 (μM) are the amplitudes of the exponential components, and α_1 and α_2 (sec^{-1}) are their rate constants.

The total ICG concentration, C_t, measured by the DOT system is a linear combination of the plasma (or intravascular) and the extravascular concentration

$$C_t = v_p C_p + v_e C_e \tag{3}$$

where v_p is the plasma fractional volume.

The solution of the equations (1) - (3) is given as (Cuccia et al. 2003)

$$\begin{aligned} C_t(t) = {} & A_1(v_p + \frac{K^{trans}}{k_{ep} - \alpha_1}) \exp(-\alpha_1 t) \\ & + A_2(v_p + \frac{K^{trans}}{k_{ep} - \alpha_2}) \exp(-\alpha_2 t) \\ & - (A_1(v_p + \frac{K^{trans}}{k_{ep} - \alpha_1}) + A_2(v_p + \frac{K^{trans}}{k_{ep} - \alpha_2})) \exp(-k_{ep} t). \end{aligned} \tag{4}$$

The rate constants k_{ep} and K^{trans} are expected to be significantly different for benign and malignant breast tumors due to increased leakiness of the blood vessels in malignant tumors (Knopp et al. 1999). In order to obtain these parameters, first the ICG concentration must be calculated from optical measurements. Then, the change in the absorption coefficient, $\delta\mu_a$, can be related to injected ICG concentration, δC, as:

$$\delta\mu_a = 2.3\varepsilon\delta C \tag{5}$$

where ε is the extinction coefficient of ICG. Then, a data fitting algorithm such as nonlinear least squares can be used to fit the calculated concentrations from equation (5) to equation (4).

2.2. Modeling of Forward and Inverse Problems

Spatially resolved absorption and scattering coefficients at different time points can be calculated from the DOT measurements solving inverse problem. In order to model the light transport in tissue, we use the diffusion equation. The frequency domain representation of the diffusion equation for the tissue is written as,

$$\bigtriangledown.D(\mathbf{r})\bigtriangledown\phi(\mathbf{r},\omega) - (\mu_a(\mathbf{r}) + \frac{i\omega n}{c_0})\phi(\mathbf{r},\omega) = -S(\mathbf{r},\omega) \tag{6}$$

where $\phi(\mathbf{r},\omega)$ is the optical light fluence rate ($W.mm^{-2}$), $S(\mathbf{r},\omega)$ is the optical light source ($W.mm^{-3}$), ω is the optical light source modulation frequency, $D(\mathbf{r})$ is the photon diffusion coefficient, μ_a is the photon absorption coefficient, c_0 is the speed of the light in vacuum, and n is the index of refraction of the medium. The diffusion coefficient is given as,

$$D(\mathbf{r}) = \frac{1}{3[\mu_a(\mathbf{r}) + \mu_s^{'}(\mathbf{r})]} \tag{7}$$

where $\mu_s^{'}$ is the reduced scattering coefficient.

Robin boundary condition (RBC) relates the optical fluence rate to optical flux at the boundary and can be written as

$$\phi(\xi,\omega) - 2AF(\xi,\omega) = 0 \tag{8}$$

where the optical flux $F(\xi,\omega) = -D(\mathbf{r})\hat{\mathbf{n}}.\bigtriangledown\phi(\xi,\omega)$, ξ is any point on the boundary $\partial\Omega$ of the domain Ω, $\hat{\mathbf{n}}$ is the outward normal vector for the boundary, and A is a constant that accounts for the internal reflection of light due to the index of refraction mismatch.

The inverse problem for the DOT is an estimation of the optical parameters by minimizing the error between the measured and calculated data:

$$\chi(\mu)^2 = \sum_{i}^{M}(\phi_{m,i} - \phi_{c,i}(\mu))^2 \tag{9}$$

where ϕ_m is the measured data, ϕ_c is the calculated data using the forward solver, M is the total number of source-detector combinations, and $\mu = \{\mu_a, \mu_s^{'}\}$. In order to find the minimum of the error function, the derivative is equated to zero and then the solution is expanded in a truncated Taylor series (Paulsen & Jiang 1995). The matrix equation to be solved can be written as

$$\triangle\,\mu = (\mathbf{J}^T\mathbf{J} + \lambda\mathbf{I})^{-1}\mathbf{J}^T(\phi_m - \phi_c) \tag{10}$$

where $J_{ij} = \frac{\partial\phi_{c,i}}{\partial\mu_j}$ is the Jacobian matrix that can be calculated using the adjoint method (Arridge & Schweiger 1995), $\triangle\mu$ is the update vector that is the difference between the true value and the estimated value of either absorption or reduced scattering coefficient, I is the identity matrix and λ is the Tikhonov regularization parameter.

The equation (10) can be solved iteratively. The regularization parameter is selected as (Franchois & Pichot 1997)

$$\lambda_i = \frac{\mathtt{Tr}((J^T J)_i)}{N} \frac{\mathtt{norm}(\chi_i)}{\mathtt{norm}(\chi_1)} \tag{11}$$

where i is the iteration number, Tr represents the trace of a matrix, and N is the number of unknowns. χ_1 is the norm of the error in the first iteration. This empirical method provides a very fast and efficient way of selecting the regularization parameter in each iteration.

The incorporation of the structural *a priori* information in the DOT reconstruction can be accomplished in several ways. We use *a priori* information in three steps in the reconstruction. Initially, the finite element mesh is segmented into a background region and a region of interest (ROI). In the first step, the initial optical parameters for different regions are found using a non-linear least square estimate algorithm (built in lsqnonlin function of MATLAB). Note that if *a priori* is not available, homogenous fitting is done to find the initial values. In the second step, a two region regularization method is employed. The selection of λ values can be achieved modifying the equation (11) for multiple regions.

$$\lambda_i^r = \frac{\mathtt{Tr}((J^T J)_i^r)}{N^r} \frac{\mathtt{norm}(\chi_i)}{\mathtt{norm}(\chi_1)} \tag{12}$$

where r denotes the region number, $\mathtt{Tr}((J^T J)_i^r)$ is the sum over the diagonal elements belonging to the region r and N^r is the number of unknowns corresponding to that region.

As the third step, the mean value of the optical parameters in each region is assigned to all elements in that region at the end of each iteration. As a result, the value of reconstructed optical parameters are very accurate as long as the boundaries of the regions are selected accurately. In determination of the ICG kinetics curves, structural *a priori* knowledge can be used to increase the spatial resolution and the accuracy of the reconstructed ICG concentration.

We use the finite element method (FEM) to solve the forward problem. The simulated measurement data was generated solving the forward problem on a fine mesh of 6785 nodes and 13056 elements. Then, a dual mesh scheme was used for all the reconstructions. The forward problem to obtain the fluence rate was solved on a mesh of 1761 nodes and 3264 first order triangular elements. A denser element distribution was used underneath the boundary to improve the accuracy close to measurement points. The sources were placed at a location $1/\mu_s^{'}$ below the surface. A coarse mesh with 289 nodes and 512 elements was generated for the reconstruction basis in order to reduce the number of unknowns.

2.3. Numerical Experiments

There are six simulations corresponding to different cases. We use a simplified notation to present different situations. (D,d,r) denotes a D-mm-diameter circular region with

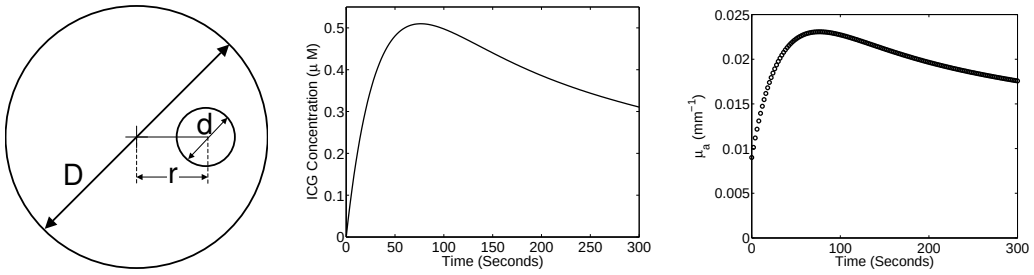

Figure 1. (a) Simulation geometry. (b) The true ICG kinetics in the simulations, and (c) the corresponding μ_a change in the ROI.

a d-mm-diameter target located r mm off-center (Figure 1a): e.g. (100,15,0) shows the case in which a 100-mm-diameter circular region with a 15-mm-diameter target located at the center of the circular region.

In the simulated cases, the time resolution was set to 16 seconds for 64 measurements. The parameters were selected as: $D = \{80, 100\}$ mm, $d = \{8, 15\}$ mm, and $r = \{0, 25\}$ mm. The background optical properties were set as $\mu_a = 0.006$ mm^{-1}, $\mu_s' = 0.8$ mm^{-1}, and $n = 1.4$. The pre-ICG optical properties of the target were set to $\mu_a = 0.009$ mm^{-1}, $\mu_s' = 1.2$ mm^{-1}, and $n = 1.4$. Single wavelength, 785 nm, and single modulation frequency, 100 MHz, were used in the simulations. Gaussian noise, 1% amplitude-noise and 0.4 degrees-phase-noise, was added to the measurement vectors in accordance with the noise levels of our experimental system. The simulated measurement data was generated by simulating a time dependent ICG concentration (Figure 1b) that caused a time dependent absorption coefficient (Figure 1c) in the ROI. Note that change in the reduced scattering due to ICG is negligible and therefore μ_s' was assumed to be constant during the simulated measurements. In order to generate the ICG kinetics, the physiological parameters k_{ep}, K^{Trans}, A_1, A_2, v_p, α_1, α_2 were assigned to be 1.56 min^{-1}, 0.348 min^{-1}, 1.5 μM, 2 μM, 0.0142, 1 min^{-1}, 0.1 min^{-1} respectively.

Absorption coefficient at different time points was calculated from the DOT measurements solving the inverse problem with and without *a priori* information. We used anatomical *a priori* information to divide the domain of interest into two distinct regions, 1) region of interest (ROI), 2) background. Then, a non-linear least squares method was used to fit the calculated concentrations within the ROI to equation (4) in order to obtain the physiological parameters. In the fitting, plasma curve rate constants and amplitudes α_1, α_2, A_1, and A_2 were fixed to 1 min^{-1}, 0.1 min^{-1}, 1.5 μM, 2.0 μM respectively. These values were selected approximately from (Shinoraha et al. 1996). As a result there were three parameters to fit in the equation (4), k_{ep}, K^{Trans}, and v_p.

2.4. Phantom Experiments

Dynamic phantom experiments were performed using two 63-mm-diameter solid phantoms that were constructed using the method described by (Firbank et al. 1996).

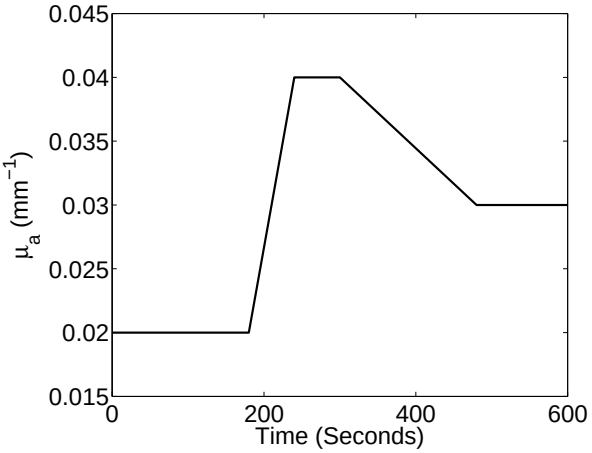

Figure 2. μ_a in the ROI was linearly increased from 0.02 to 0.04 mm^{-1} in one minute by injecting ink. After waiting for one minute, it was linearly decreased from 0.04 to 0.03 mm^{-1} in three minutes by pouring intralipid-ink mixture.

One of the phantom was homogeneous and it was used for calibration. The other phantom that was designed for DCE-DOT phantom studies had a cylindrical inclusion (Gulsen et al. 2007). The diameter of the inclusion was 15 mm and it was located at the midway between the center and the edge. The phantoms had optical properties of $\mu_a = 0.013\ mm^{-1}$ and $\mu_s' = 0.8\ mm^{-1}$. The details of our imaging system and the calibration procedure can be found in (Gulsen et al. 2006) and (Unlu et al. 2006).

Initially, a dye-intralipid-water mixture which had optical properties of $\mu_a = 0.02$ (mm^{-1}) and $\mu_s' = 0.8$ (mm^{-1}) was circulated through the phantom using a metering pump. The main solution was kept in a container. After the baseline measurements, a computer controlled syringe pump was used to inject Indian-ink into the container to increase the absorption coefficient linearly up to 0.04 mm^{-1} in one minute (Figure 2). Simultaneously, a stirrer was used to mix the solution in the container and the pump continued circulating the solution throughout the experiment. After the injection was finished, we waited for one minute, then started the dilution using another container with a pump by pouring intralipid-water mixture to the main container. The dilution lasted three minutes. A complete set of DOT data of 64 measurements was acquired in 30 seconds. To increase the temporal resolution, only a single modulation frequency, 100 MHz, was employed. 20 DOT data sets were acquired in approximately 10 minutes at 785 nm.

3. Results

3.1. Simulation Results

We performed the reconstructions for the baseline measurements for all six cases. In baseline simulations, absorption coefficient was static in time and scattering map was also reconstructed. For example, Figure 3 shows the reconstructed optical parameter

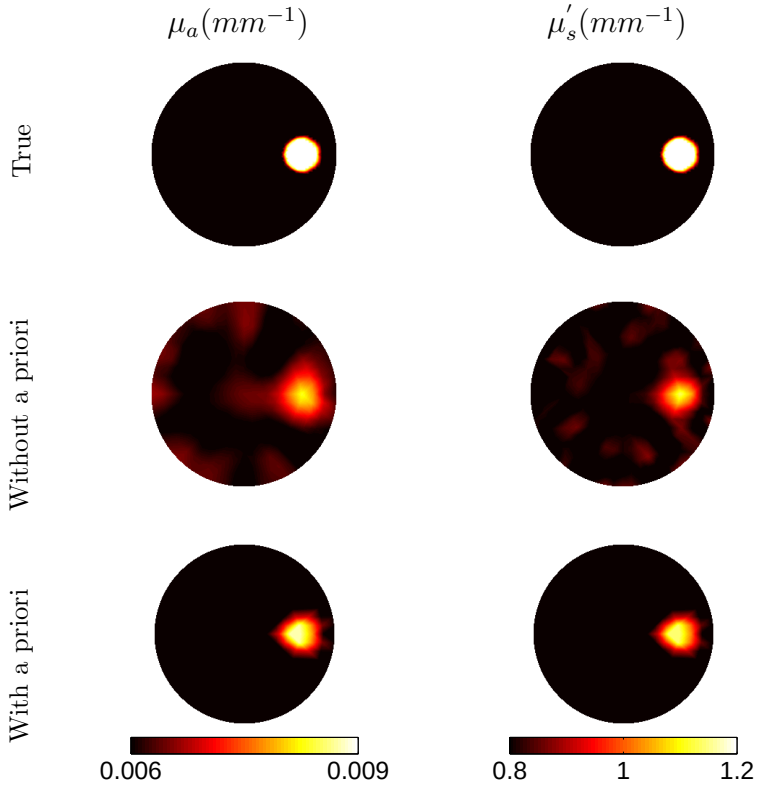

Figure 3. Reconstructed optical parameters for baseline measurements for the case (80,15,25). First row shows the true optical parameter distributions, second row shows the reconstruction without *a priori* knowledge, and the third row shows the reconstruction with *a priori* knowledge of the location of the inclusion.

maps for the simulated baseline data for (80,15,25) case. The reconstructions were performed without (second row) and with (third row) structural priors. The errors in calculated maximum values of μ_a and $\mu_s^{'}$ in the ROI were within 5% of the true value in both reconstructions with and without structural priors.

In the next step, the dynamic simulations were performed for all cases to calculate the absorption coefficient at each time point in the ROI. For example, Figure 4 shows the reconstructed optical parameter maps at three time points for the simulated dynamic data for (80,15,25) case. The reconstructions were performed without (first row) and with (second row) structural priors.

Afterwards, we calculated the peak ICG concentration, K^{trans}, k_{ep}, and v_p for each simulation case. The peak concentrations of the inclusions had large errors (Table 1). For example, the fitting of the peak concentration resulted 66% error in $(80, 15, 25)$ case, 84% error in $(100, 8, 25)$ and 58% error in $(80, 15, 0)$ case. However, when the structural priors were used, the errors reduced to 6%, 39% and 1% respectively. On the other hand, the peak concentration values were different for each case and the reconstructions resulted in different peaks although the true peak was same for all (Figure 5). This was an expected result and showed that the calculated peak concentration was dependent

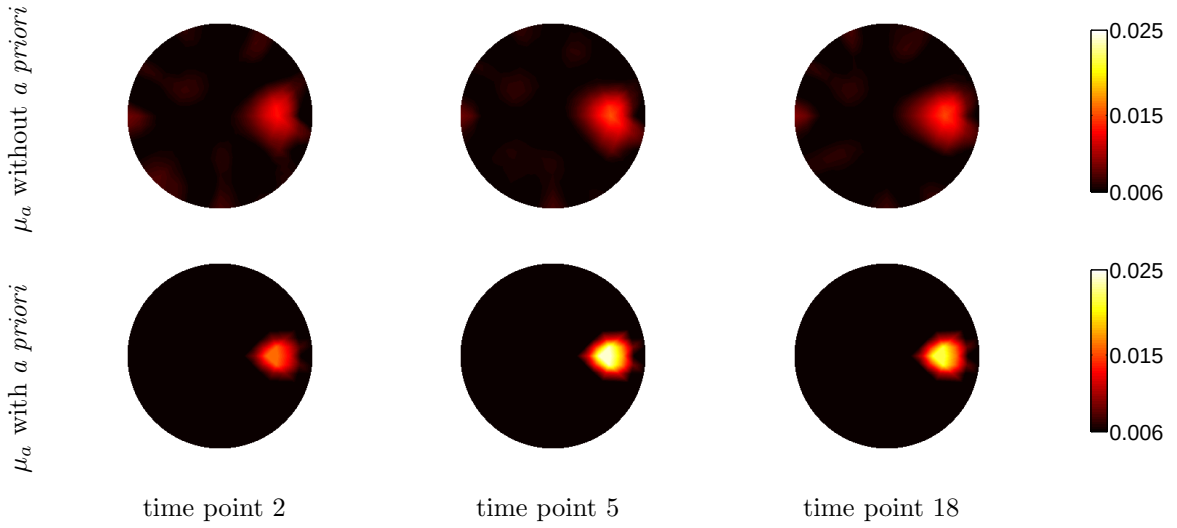

Figure 4. Reconstructed optical parameter at three time points for the case (80,15,25). First row shows the reconstructions without using *a priori* knowledge and the second row shows the reconstructions using *a priori* knowledge of the location of the inclusion.

Table 1. The percentage error in peak ICG concentration in each case.

Case	Error in peak ICG	
	Without *a priori*	With *a priori*
(100,15,0)	74%	6 %
(100,8,25)	84%	39%
(100,15,25)	72%	9%
(80,15,0)	58%	1%
(80,15,25)	66%	6%
(80,8,25)	78%	31%

on the size and the location of the inclusion as well as the size of the imaging region.

In Table 2, the calculated fitting parameters and the corresponding standard deviations and the coefficient of variations are summarized. In this case, no structural priors were used in the calculation of absorption coefficient. The fitting results ranged from 0.0112 to 0.0793 (sec^{-1}) for k_{ep} and from 0.0008 to 0.0032 sec^{-1} for K^{trans}. For example, the fitted values of k_{ep} and K^{trans} were 0.0147 sec^{-1} and 0.0009 sec^{-1} respectively in $(80, 15, 25)$ situation. We also calculated the coefficient of variation that was defined as standard deviation divided by mean. The coefficients of variation for k_{ep}, K^{trans}, and v_p were 60%, 95%, and 114% respectively. Note that, huge errors in the ICG curves could be seen in the first row of the Figure 5. Especially, the calculated values of the time to reach the peak ICG concentration for 8-mm inclusion and 15-mm inclusion were very different. However, the coefficients of variation for k_{ep}, K^{trans}, and v_p were reduced to 29%, 15%, 93% when the *a priori* information was used in

Table 2. The calculated physiological parameters and their variability. In the DOT reconstruction *a priori* information was not used.

Case	K^{Trans} (sec^{-1})	k_{ep} (sec^{-1})	v_p
True value	0.0058	0.026	0.0142
(100,15,0)	0.0008	0.0118	0.0110
(100,8,25)	0.0022	0.0112	0.0090
(100,15,25)	0.0009	0.0125	0.0114
(80,15,0)	0.0032	0.0357	0.0001
(80,15,25)	0.0009	0.0147	0.0436
(80,8,25)	0.0030	0.0793	0.0060
Mean	0.0018	0.0442	0.0135
Standard deviation	0.0011	0.0418	0.0153
Coefficient of variation	60%	95%	114%

Table 3. The calculated physiological parameters and their variability. In the DOT reconstruction *a priori* information was used.

Case	K^{Trans} (sec^{-1})	k_{ep} (sec^{-1})	v_p
True value	0.0058	0.026	0.0142
(100,15,0)	0.0058	0.0242	0.0158
(100,8,25)	0.0025	0.0158	0.0082
(100,15,25)	0.0044	0.0201	0.0109
(80,15,0)	0.0045	0.0203	0.0382
(80,15,25)	0.0044	0.0182	0.002
(80,8,25)	0.0031	0.0179	0.0099
Mean	0.0041	0.0194	0.0139
Standard deviation	0.0012	0.0029	0.0130
Coefficient of variation	29%	15%	93%

DOT reconstruction (Table 3). As a result, when the ICG curves were normalized with respected to their maximum values, they overlaid on top of each other (the second row of Figure 5). This showed that the use of structural priors reduced the effects of random and systematic errors on the calculation of ICG curves and the rate constants K^{trans} and k_{ep} were independent of target size, location, and size of the imaging region. Note that v_p was not improved much when the structural priors were used. Therefore it might be useful to calculate this value using the baseline measurements as suggested by (Cuccia et al. 2003).

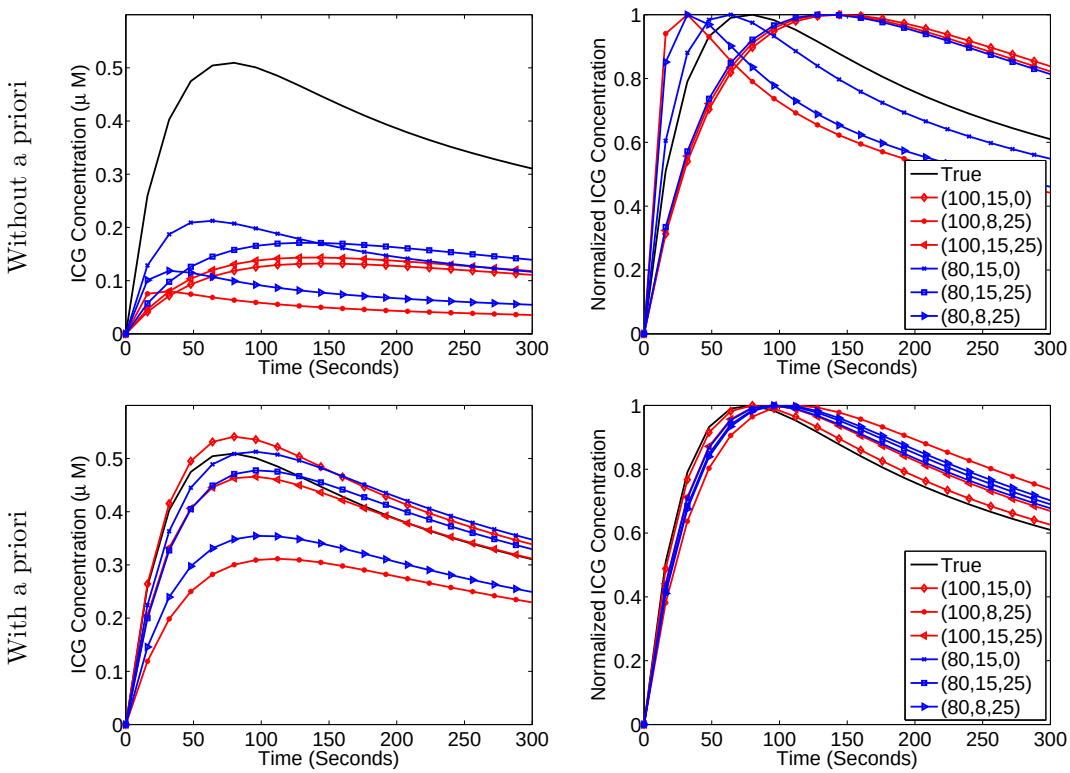

Figure 5. Comparison of ICG and normalized ICG curves in two circular regions. i.e. (100,15,25) denotes a 100-*mm*-diameter circular region with a 15-*mm*-diameter target located 25 *mm* away from the center. First row: No structural priors were used in the calculation of optical parameters, and as a result the calculated ICG kinetics had gross errors. Second row: Structural priors were used. The shape of the ICG kinetics was recovered accurately.

3.2. The Results of Phantom Experiments: Validation of the Use of Structural Priors

Figure 6a shows the true absorption coefficient change in the ROI and the one measured by DOT. Two curves overlay on top of each other if they are normalized to their maximum values (Figure 6b). This shows that the DCE-DOT system accurately acquired the injection and the dilution rates. However, the peak absorption coefficient was below the expected value. One reason for this might be the error in the preparation of the dye-intralipid-water mixture.

In order to validate the use of structural priors in DCE-DOT, errors were incorporated in the selection of ROI during the reconstruction. Figure 7 shows the absorption curves obtained by four different segmentations. In the first case, reconstructions were performed assuming we had the true knowledge of the size and location of the inclusion. In the next two cases, the diameter of the inclusion was selected 20% and 30% larger than the true diameter and in the last case, the inclusion was 30% misplaced toward the center of the imaging region. The data fitting was performed accordingly for all cases. Considering that the true diameter of the inclusion was 15 *mm*, huge errors occurred in the calculated peak absorption coefficient even

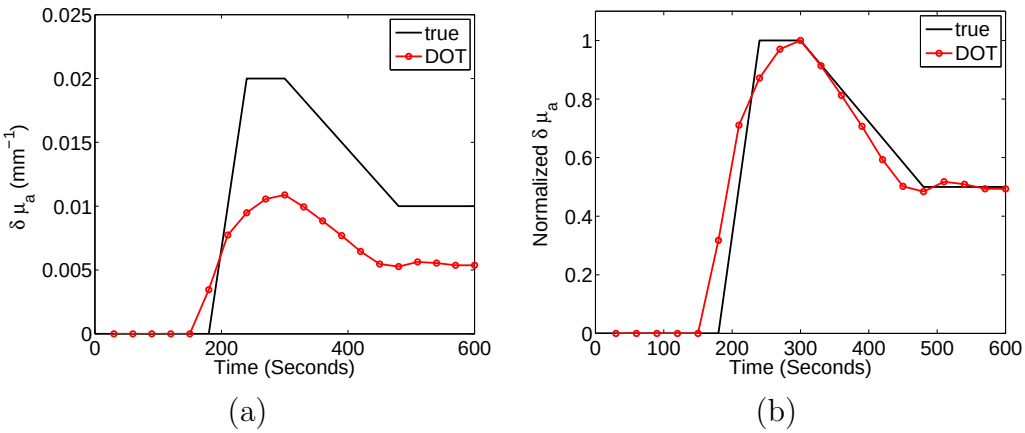

Figure 6. Comparison of the true change in absorption coefficient in the ROI with the DOT measurements.

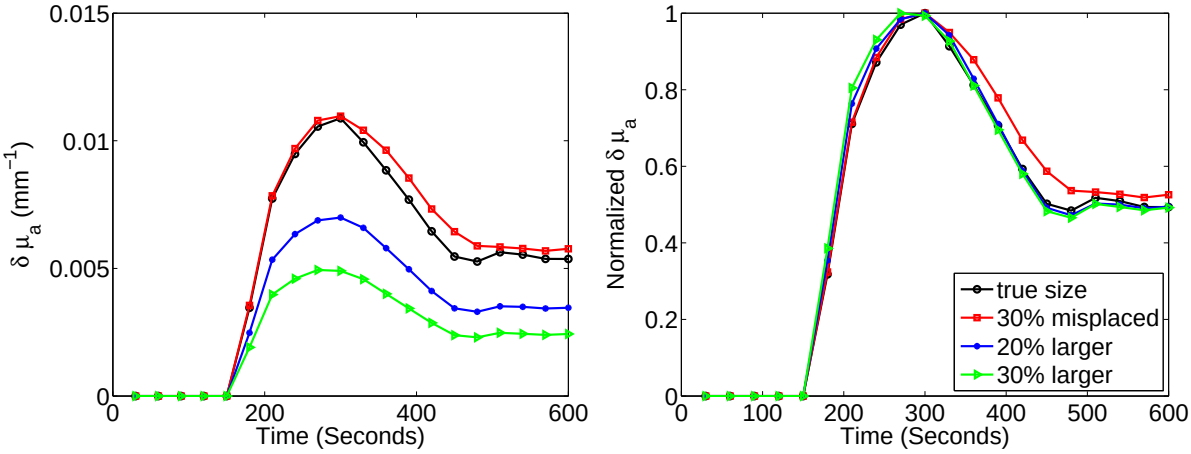

Figure 7. The effect of wrong segmentation on the calculated ICG curve.

though baseline correction was applied. However, the normalized curves overlaid on top of each other. Therefore, the rate constants were immune to systematic errors caused by incorrect structural *a priori* information. To illustrate this, we calculated the injection and dilution rates from the normalized absorption curves (Table 4) by calculating the rising up slope and falling down slope respectively. Misplacing the inclusion by 30% caused a 1% change in injection and 6% change dilution rate. Similarly, 20% and 30% error in the selection of the size of the inclusion caused 0.1% and 2% change in the injection rate, 7% and 4% change in the dilution rate respectively.

4. Discussion and Conclusions

In summary, we used a frequency domain DOT system to measure ICG kinetics. We performed simulation and phantom studies. In the simulations, we used a two-compartmental model to fit the physiological parameters and analyzed the effects of limitations of DOT in measurements of these parameters. We calculated ICG curves

Table 4. The percentage change in the calculated injection and dilution rate due to the errors in the selection of structural priors.

Case	Change in Injection Rate (%)	Change in Dilution Rate (%)
30% misplaced	1%	6%
20% larger	0.1%	7%
30% larger	2%	4%

by varying the size of the imaging region, the size and the location of the inclusion. Although the ICG kinetics were same for all of them, the calculated kinetics were different in each case. Especially, when the structural priors were not used in the calculation of optical parameters, the calculated K^{trans}, k_{ep}, and v_p values had large variations among different cases. As a result, time to reach the peak ICG concentration showed significant variations within different cases. However, when the structural *a priori* was used, these variations were reduced and when the ICG curves were normalized with respected to their maximum values, they overlaid on top of each other. This showed that the wash-in, K^{trans}, and wash-out, k_{ep} rates were independent of intra-subject and inter-subject differences in DCE-DOT measurements if structural *a priori* information were used. In addition to this, we showed that the absolute peak concentration value depends on the size and the location of the inclusion and the size of imaging region. Therefore, peak concentration was not an informative parameter when it was used to make comparisons between different cases. This was previously mentioned by (Alacam, Yazici, Intes & Chance 2006).

In addition to simulations, we also performed a phantom experiment. In this experiment, we investigated the use of structural *a priori* information in DCE-DOT reconstruction and corresponding effects on the calculation of physiological parameters. We showed that the wash-in and wash-out parameters were immune to errors in the selection of structural priors. On the other hand, the calculated peak concentration was sensitive to the selection of the structural priors. This was in agreement with the findings of (Dehghani et al. 2006).

The analysis presented in this study shows that the ICG kinetics curves obtained by a frequency domain DOT system have the potential to characterize the tumor permeability. The optical imaging system described above is a low cost system and can be integrated with available MR systems with proper modifications. Such a hybrid system that can monitor the enhancement kinetics of an MR (Gd-DPTA) and an optical (ICG) contrast agent has a great potential for increasing specificity in tumor characterization.

Acknowledgments

We thank to Min-Ying Su and Hon J. Yu for their discussions on the subject. This research is supported in part by the National Cancer Institute through Grant # R21/33

CA-101139, the California Breast Cancer Research Program No. 12IB-0095, and U.S. Army BC051304.

References

Alacam B, Yazici B, Intes X & Chance B 2005 *Conf Proc IEEE Eng Med Biol Soc* **1**, 62–65.

Alacam B, Yazici B, Intes X & Chance B 2006 *IEEE Trans Biomed Eng* **53**, 1861–1871.

Alacam B, Yazici B, Intes X, Nioka S & Chance B 2006 *Imaging, manipulation, and Analysis of Biomolecules, Cells, and Tissues IV, Proc. of SPIE* **6088**, 60881N.

Arridge S R & Schweiger M 1995 *Applied Optics* **34**, 8026–8037.

Brooksby B, Srinivasan S, Jiang S, Dehghani H, Pogue B W, Paulsen K D, Weaver J, Kogel C & Poplack S P 2005 *Opt Lett* **30**(15), 1968–1970.

Cerussi A, Shah N, Hsiang D, Durkin A, Butler J & Tromberg B J 2006 *J Biomed Opt* **11**(4), 044005.

Cuccia D J, Bevilacqua F, Durkin A J, Merritt S, Tromberg B J, Gulsen G, Yu H, Wang J & Nalcioglu O 2003 *Appl Opt* **42**(16), 2940–2950.

Dehghani H, Carpenter C M, Yalavarthy P K, Pogue B W & Culver J P 2006 *in* 'Multimodel Biomedical Imaging II, Proc. Of SPIE'.

Dehghani H, Pogue B W, Shudong J, Brooksby B & Paulsen K D 2003 *Appl Opt* **42**(16), 3117–3128.

Ferrari M 2005 *Nat Rev Cancer* **5**(3), 161–171.

Firbank M, Arridge S R, Schweiger M & Delpy D T 1996 *Phys Med Biol* **41**(4), 767–783.

Franchois A & Pichot C 1997 *IEEE Transactions on Antennas and Propagation* **45**, 203–215.

Gibson A P, Hebden J C & Arridge S R 2005 *Phys Med Biol* **50**(4), R1–43.

Gulsen G, Unlu M B, Birgul O & Nalcioglu O 2007 Vol. 6431 SPIE p. 64310D.

Gulsen G, Xiong B, Birgul O & Nalcioglu O 2006 *J Biomed Opt* **11**(1), 014020.

Gurfinkel M, Thompson A B, Ralston W, Troy T L, Moore A L, Moore T A, Gust J D, Tatman D, Reynolds J S, Muggenburg B, Nikula K, Pandey R, Mayer R H, Hawrysz D J & Sevick-Muraca E M 2000 *Photochem Photobiol* **72**(1), 94–102.

Intes X, Maloux C, Guven M, Yazici B & Chance B 2004 *Phys Med Biol* **49**(12), N155–N163.

Intes X, Ripoll J, Chen Y, Nioka S, Yodh A G & Chance B 2003 *Med Phys* **30**(6), 1039–1047.

Jain K K 2005 *Clin Chim Acta* **358**(1-2), 37–54.

Knopp M V, Weiss E, Sinn H P, Mattern J, Junkermann H, Radeleff J, Magener A, Brix G, Delorme S, Zuna I & van Kaick G 1999 *J Magn Reson Imaging* **10**(3), 260–266.

Li A, Miller E L, Kilmer M E, Brukilacchio T J, Chaves T, Stott J, Zhang Q, Wu T, Chorlton M, Moore R H, Kopans D B & Boas D A 2003 *Appl Opt* **42**(25), 5181–5190.

Li C, Liengsawangwong R, Choi H & Cheung R 2007 *Med Phys* **34**(1), 266–274.

Malicka J, Gryczynski I, Geddes C D & Lakowicz J R 2003 *J Biomed Opt* **8**(3), 472–478.

Mourant J R, Hielscher A H, Eick A A, Johnson T M & Freyer J P 1998 *Cancer* **84**(6), 366–374.

Ntziachristos V, Yodh A G, Schnall M & Chance B 2000 *Proc Natl Acad Sci U S A* **97**(6), 2767–2772.

Paulsen K D & Jiang H 1995 *Med Phys* **22**(6), 691–701.

Pogue B, Song X, Tosteson T, McBride T, Jiang S & Paulsen K 2002 *Medical Imaging, IEEE Transactions on* **21**(7), 755–763.

Pogue B W, Davis S C, Song X, Brooksby B A, Dehghani H & Paulsen K D 2006 *J Biomed Opt* **11**(3), 33001.

Pogue B W, Willscher C, McBride T O, Osterberg U L & Paulsen K D 2000 *Med Phys* **27**(12), 2693–2700.

Shinoraha H, Tanaka A, Kitai T, Yanabu N, Inomoto T, Satoh S, Hatano E, Yamaoka Y & Hirao K 1996 *Hepatology* **23**, 137–144.

Song X, Pogue B W, Tosteson T D, McBride T O, Jiang S & Paulsen K D 2002 *IEEE Trans Med Imaging* **21**(7), 764–772.

Thomsen S & Tatman D 1998 *Ann N Y Acad Sci* **838**, 171–193.

Tofts P S & Kermode A G 1991 *Magnetic Resonance in Medicine* **17**, 357.

Unlu M B, Birgul O, Shafiiha R, Gulsen G & Nalcioglu O 2006 *J Biomed Opt* **11**(5), 054008.
Yezhelyev M V, Gao X, Xing Y, Al-Hajj A, Nie S & O'Regan R M 2006 *Lancet Oncol* **7**(8), 657–667.
Yoneya S, Saito T, Komatsu Y, Koyama I, Takahashi K & Duvoll-Young J 1998 *Invest Ophthalmol Vis Sci* **39**(7), 1286–1290.